Monthly Notices
of the
ROYAL ASTRONOMICAL SOCIETY

MNRAS **496,** 138–151 (2020)
Advance Access publication 2020 May 30

doi:10.1093/mnras/staa1488

VLA and ALMA observations of the lensed radio-quiet quasar SDSS J0924+0219: a molecular structure in a 3 μJy radio source

Shruti Badole [1]★ Neal Jackson,[1] Philippa Hartley,[1,2] Dominique Sluse,[3] Hannah Stacey [4,5,6] and Héctor Vives-Arias [7,8]

[1]*Jodrell Bank Centre for Astrophysics, Department of Physics & Astronomy, University of Manchester, Alan Turing Building, Oxford Road, Manchester M13 9PL, UK*
[2]*Square Kilometre Array Organisation, Macclesfield, Cheshire SK11 9DL, UK*
[3]*STAR Institute, Quartier Agora – Allée du six Août, 19c B-4000 Liège, Belgium*
[4]*ASTRON, Netherlands Institute for Radio Astronomy, Oude Hoogeveensedijk 4, NL-7991 PD Dwingeloo, the Netherlands*
[5]*Kapteyn Astronomical Institute, PO Box 800, NL-9700 AV Groningen, the Netherlands*
[6]*Max Planck Institute for Astrophysics, Karl-Schwarzschild Str 1, D-85748 Garching bei München, Germany*
[7]*Instituto de Astrofísica de Canarias, Vía Láctea, s/n, E-38205 La Laguna, Tenerife, Spain*
[8]*Departmento de Astrofísica, Universidad de La Laguna, E-38205 La Laguna, Tenerife, Spain*

Accepted 2020 May 21. Received 2020 May 21; in original form 2019 October 23

ABSTRACT

We present Karl G. Jansky Very Large Array (VLA) and Atacama Large Millimetre Array (ALMA) observations of SDSS J0924+0219, a $z = 1.524$ radio-quiet lensed quasar with an intrinsic radio flux density of about 3 μJy. The four lensed images are clearly detected in the radio continuum and the CO(5–4) line, whose centroid is at $z = 1.5254 \pm 0.0001$, with a marginal detection in the submillimetre continuum. The molecular gas displays ordered motion, in a structure approximately 1–2.5 kpc in physical extent, with typical velocities of 50–100 km s^{-1}. Our results are consistent with the radio emission being emitted from the same region, but not with a point source of radio emission. SDSS J0924+0219 shows an extreme anomaly in the flux ratios of the two merging images in the optical continuum and broad emission lines, suggesting the influence of microlensing by stars in the lensing galaxy. We find the flux ratio in the radio, submillimetre continuum and CO lines to be slightly greater than 1 but much less than that in the optical, which can be reproduced with a smooth galaxy mass model and an extended source. Our results, supported by a microlensing simulation, suggest that the most likely explanation for the optical flux anomaly is indeed microlensing.

Key words: gravitational lensing: strong – quasars: individual: SDSS J0924+0219 – galaxies: star formation.

1 INTRODUCTION

In a strong gravitational lensing system, the light from a background source is deflected due to the gravitational potential of a foreground galaxy or galaxy cluster, resulting in multiple images of the background source. The position and brightness of the lensed images contain information about the structure of the source, together with the mass distribution of the lensing galaxy (Treu 2010). Lensing galaxies or galaxy clusters also magnify the sources by factors of typically 10–20, allowing us to study lensed sources that would otherwise be unobservably faint (Yuan et al. 2012; Zheng et al. 2012; Atek et al. 2015).

The use of effective increases in resolution and/or sensitivity is particularly interesting in sources which contain a quasar. About 10 per cent of quasars are radio loud, with the radio synchrotron emission being generated by jets ejected from close to the central black hole. The remainder generally have weak radio emission, which may be a result of jet activity similar to that in radio loud quasars but on a smaller scale (Herrera Ruiz et al. 2016; Zakamska et al. 2016; White et al. 2017; Hartley et al. 2019; Jarvis et al. 2019), or due to processes associated with star formation (Condon et al. 2013; Bonzini et al. 2015; Padovani et al. 2017; Stacey et al. 2019). One way to investigate this question is to study the molecular gas component associated with star formation processes; this can be detected using molecular lines in the sub-millimetre part of the spectrum, and its morphology and extent compared with the radio continuum. The question of the interaction between active galactic nucleus (AGN) and star-forming components is important because it has been suggested for some time (e.g. Croton et al. 2006) that AGNs are responsible for regulating star formation in galaxies, periodically clearing out gas in order to stop star formation. More

★ E-mail: shruti.badole@postgrad.manchester.ac.uk

complex regulatory interactions have also been proposed (Maiolino et al. 2017).

The study of molecular gas in lensed submillimetre galaxies has a long history (for recent examples, see e.g. Hezaveh et al. 2013b; Rybak et al. 2015; Aravena et al. 2016; Yang et al. 2017; Geach et al. 2018). Molecular gas reservoirs have also been found in quasars (Riechers et al. 2009a; Tuan-Anh et al. 2017; Paraficz et al. 2018). We can use lens models to correct for the lensing magnification and derive the intrinsic CO luminosity in these objects, and also estimate the molecular gas mass if we assume the quantity α_{CO}, which relates CO to overall molecular gas mass, is similar to more directly accessible objects (Venturini & Solomon 2003; Riechers et al. 2009a, 2011; Deane et al. 2013; Tuan-Anh et al. 2017). More recently, detailed imaging together with lens inversion has been used to calculate values for α_{CO} and reconstruct lensed sources in more detail (Paraficz et al. 2018; Spingola et al. 2019).

Imaging of radio structures in lensed radio-quiet quasars has also been recently developed, with a number of detections of spatially resolved radio emission (Wucknitz & Volino 2008; Jackson 2011; Jackson et al. 2015; Hartley et al. 2019). In cases such as RXJ 1131−1231, high-resolution radio observations resolve out the emission, suggesting emission from an extended disc (Wucknitz & Volino 2008); in others, variability or directly imaged core-jet structures with very long baseline interferometry (VLBI) suggest AGN origin as in HS 0810+2554 (Hartley et al. 2019). The latter is a surprising result because the object lies within the scatter of the far-infrared (FIR)–radio correlation resulting from the comparison of lensed radio and *Herschel* far-infrared luminosities in a large sample of lensed quasars (Stacey et al. 2018), where both radio and FIR emission are expected to be produced by the same, star formation, mechanism. There is thus a strong motivation to investigate in detail both radio and sub-millimetre emission in the same objects, to derive clues on the relation between radio-emitting components and the molecular gas.

For smooth lens potentials, a point source near a fold or cusp caustic should yield well-defined flux ratios. For fold systems such as SDSS J0924+0219, the two close images of a point source should have the same brightness; deviations from this may indicate millilensing by clumped matter distributions in the lensing galaxy close to the line of sight to one or both of the images (Fassnacht et al. 1998; Mao & Schneider 1998; Metcalf & Madau 2001; Chiba 2002; Dalal & Kochanek 2002; Metcalf & Zhao 2002; Saha, Williams & Ferreras 2007; Kratzer et al. 2011). The mass scale to which these flux anomalies are sensitive can be as small as 10^6 $M_\odot$, sufficient to distinguish between cold dark matter (CDM) and warm dark matter (WDM) (Miranda & Macciò 2007; Gilman et al. 2019). At larger scales, gravitational imaging of optically bright lens systems with extended sources has been used to more directly detect the influence of $\sim 10^9$ $M_\odot$ substructure (Vegetti & Koopmans 2009; Vegetti, Czoske & Koopmans 2010a; Vegetti et al. 2010b; Hezaveh et al. 2016).

Studies (e.g. Xu et al. 2012) also attribute the flux anomaly to structures present along the line of sight to the primary lens and other factors such as propagation effects (Xu et al. 2015). It has been found that anomalies could also be caused by extended sources (Amara et al. 2006; Jackson et al. 2015), or edge-on disc components in the lensing galaxy (Möller, Hewett & Blain 2003; Hsueh et al. 2016).

In addition to millilensing effects, optical sources can also be prone to producing measurable flux variation in the lensed images due to microlensing by stars in the lensing galaxy (Chang & Refsdal 1979). Anomalous flux ratios due to microlensing by stars in the lensing galaxy have been found in many systems (e.g. Irwin et al. 1989; Witt, Mao & Schechter 1995; Burud et al. 2002; Vuissoz et al. 2007; Poindexter, Morgan & Kochanek 2008; Vuissoz et al. 2008); typically, monitoring of lensed quasars over the time range of years is essential to identify the effects of microlensing.

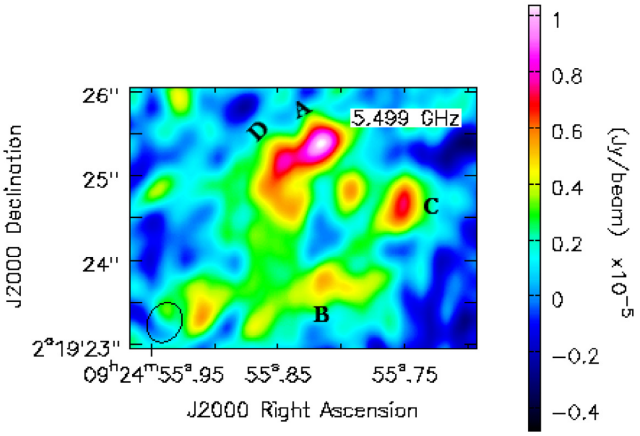

Figure 1. Map of SDSS J0924+0219 from the Very Large Array. The map is the coadded version of all four 3-h observing chunks. All four images of the lensed source are clearly detected, with a measured map noise level of 1.3 μJy beam^{-1}. The flux density of the lensing system in the map is 90 ± 9.1 μJy, assuming a 10 per cent flux calibration accuracy. The beam size is 0.489 arcsec × 0.395 arcsec with position angle of −28.43°.

The sample of strong lenses is currently dominated by those lenses where the source is an optically selected quasar, so only a small (≃10 per cent) subset of these samples have been used for substructure studies. Measurements at longer wavelengths, where the continuum source size is ≫1 μas and not subject to microlensing, are important (Chiba et al. 2005; Fadely & Keeton 2011, 2012; Hezaveh et al. 2013a; Jackson et al. 2015; Hartley et al. 2019) as are studies of the extended optical narrow emission lines (Moustakas & Metcalf 2003; Sugai et al. 2007; Nierenberg et al. 2017, 2020).

1.1 The quasar SDSS J0924+0219

SDSS J0924+0219 was discovered by Inada et al. (2003) as part of the Sloan Digital Sky Survey Quasar Lens Search (SQLS) and consists of a radio-quiet quasar at $z = 1.524$ quadruply imaged by an early-type galaxy at $z = 0.394$ (Eigenbrod et al. 2006). It was selected for observation due to an unusually large flux anomaly: it is a fold-configuration lens, but the pair of merging images, A and D in Fig. 1, has a brightness ratio in the optical waveband of 12:1 (Inada et al. 2003). Spectroscopy using the *Hubble Space Telescope* (Keeton et al. 2006) revealed the presence of flux anomaly in the broad emission line flux ratios, with the continuum and broad line emission flux ratios in the merging images being 19 and 10, respectively. This analysis also suggested the presence of microlensing in the lens system (see also Morgan et al. 2006). The microlensing duration expected for the lens in this system is 0.39 yr and the duration averaged over a sample of 87 lenses is 7.3 months (Mosquera & Kochanek 2011). However, the anomaly in SDSS J0924+0219 has persisted for 15 yr now (Faure et al. 2011; MacLeod et al. 2015), which is an unusual time-scale for microlensing to occur (Peeples, Schechter & Wambsganss 2004 and Morgan et al. 2006 predicted brightening of the demagnified image over the time-scale of roughly a decade). Such an extreme flux

Table 1. Summary of observations of SDSS J0924+0219 on the VLA.

Parameter	Values
Proposal code	AJ413
Observation dates	2018 April 4, 6–8
Configuration	A
Central frequency	5.5 GHz
Bandwidth	2 GHz
Flux density	90 ± 9.1 μJy

anomaly over such a long period of time[1] suggests the possibility that it could be driven by not only microlensing but also other factors such as millilensing by substructure.

We observed SDSS J0924+0219 in order to investigate the properties of the radio and molecular gas reservoirs in the source, and investigate the causes of the flux anomaly further. This paper is divided into four sections. Section 2 discusses the Karl G. Jansky Very Large Array (VLA) and Atacama Large Millimetre Array (ALMA) observations in the radio and submillimetre wavebands, and the initial data reduction carried out using the calibration pipelines of the observatories. Section 3 discusses the data analysis in the image plane and the $u - v$ plane, followed by Section 4 that discusses the nature of the radio source and the flux anomaly in SDSS J0924+0219. Where necessary we assume a flat Universe with $H_0 = 68.3$ km s^{-1} Mpc^{-1} and $\Omega_m = 0.3$; for the source this gives a luminosity distance $D_L = 11\,400$ Mpc and an angular size distance $D_A = 1790$ Mpc. 1 mas corresponds to 8.6 pc at the redshift of this source.

2 OBSERVATIONS AND DATA PROCESSING

2.1 VLA observations

SDSS J0924+0219 was observed using the VLA in the A configuration, providing a maximum baseline of 36 km and resolution of 350 mas at 5 GHz. The observation was made under proposal code AJ413 (PI Jackson) in the *C* band (4.488–6.512 GHz) with a total bandwidth of 2 GHz using 16 IFs of 128 MHz each. Twelve hours of observations were divided into four blocks of three hours each, which were observed on 2018 April 4, 6, 7, and 8. The observation log is summarized in Table 1.

J0914+0245 and J1331+3030 (3C 286) were used as the phase and the flux calibrators, respectively. Each of the 3-h blocks contained 2 h 10 m of on-source observation and 32 min on the phase calibrator; the phase calibrator was observed for 2 min in each 10-min cycle, followed by 8 min of the target observation.

The VLA Calibration Pipeline, using the software package CASA (Common Astronomy Software Application[2]; Mcmullin et al. 2007) was run on each of the four measurement sets. The pipeline applies basic radio frequency interference (RFI) flagging to the data, derives the initial and final delay, bandpass, and gain/phase calibrations, determines the overall flux scale of the data using the flux calibrator (J1331+3030 in this case) and also creates images of the calibrators. We combined the calibrated measurement sets generated by the pipeline and imaged the lensed source using the CLEAN algorithm (Högbom 1974) implemented in CASA with natural weighting. The final map is shown in Fig. 1. The overall off-source noise level in the map is 1.3 μJy beam^{-1}, which is in agreement with the expected noise level of 1.1–1.3 μJy beam^{-1} with natural weighting. The peak signal level of the map is about eight times the noise level.

[1]The more recent photometry by Gaia Data Release 2 (Gaia Collaboration 2018) shows persistence of the flux ratio anomaly.

[2]Distributed by the National Radio Astronomy Observatory; http://casa.nrao.edu.

Table 2. Summary of observations of SDSS J0924+0219 on ALMA.

Parameter	Values
Project code	2018.1.01447.S
Observation date	2018 Dec. 19
Maximum baseline length	500 m
Spectral windows frequencies	226, 228, 242, 244 GHz
Total bandwidth	8 GHz
CO(5–4) peak flux density	3.9 mJy beam^{-1}
CO(5–4) FWHM	200.02 ± 6.57 km s^{-1}
CO(5–4) luminosity, $\mu L'_{CO}$	3.16×10^{10} K km s^{-1} pc^2

2.2 ALMA observations

ALMA observations (Table 2) were performed on 2018 December 19 (project code 2018.1.01447, PI Jackson) using 45 antennas of the 12-m array, centred on the source SDSS J0924+0219. Five minutes of on-source integration time were obtained, with observations being performed on the nearby sources J0854+2006 and J0930+0034 for amplitude and phase calibration, respectively. The observations were reduced by the standard ALMA pipeline system using the CASA data analysis package. Observations were performed in four spectral windows close to frequencies of 226, 228, 242, and 244 GHz; the second window was expected to contain the redshifted CO(5–4) line which has a rest frequency of 576.36 GHz and therefore an expected observed frequency of 228.35 GHz given the published redshift of 1.524. Each spectral window was divided into 128 15.6-MHz channels. The array configuration used gave a resolution of approximately 0.8 arcsec with natural weighting; the calibrated data were also re-imaged with Briggs weighting (with a default robustness parameter of 0.0), giving a higher resolution of 0.68 arcsec × 0.56 arcsec with PA = 69.77°, with only marginal increase in noise level. A VLA image was also created, for comparison purposes, with a beam convolved to match the Briggs-weighted ALMA image.

In this very short observation, we achieve noise levels of 0.2 mJy beam^{-1} in each spectral window, or 0.1 mJy beam^{-1} overall. We detect the submillimetre continuum at a level of approximately 2 mJy within an area encompassing all four lensed images, but with the signal-to-noise available it is not possible to make sensible measurements of the individual component fluxes. Fig. 2 shows the map of the continuum obtained by cleaning the line-free spectral windows in the ALMA data. The CO(5–4) line is clearly detected in all four components, and the integrated line flux density, with the continuum subtracted, is also shown in Fig. 2 (left). The peak signal-to-noise ratio of the CO(5–4) line map is 19.5. Fig. 3 shows the same map in greyscale with the radio contours overlaid on top; there is a clear similarity between the two maps. A more quantitative comparison of the two maps can be seen in Fig. 4, which shows the CO line emission map divided by the radio map (convolved down to the ALMA beam). The radio and CO emission in the A and D regions appear indistinguishable, suggesting that the CO and the radio emission originate at least in part from the same region.

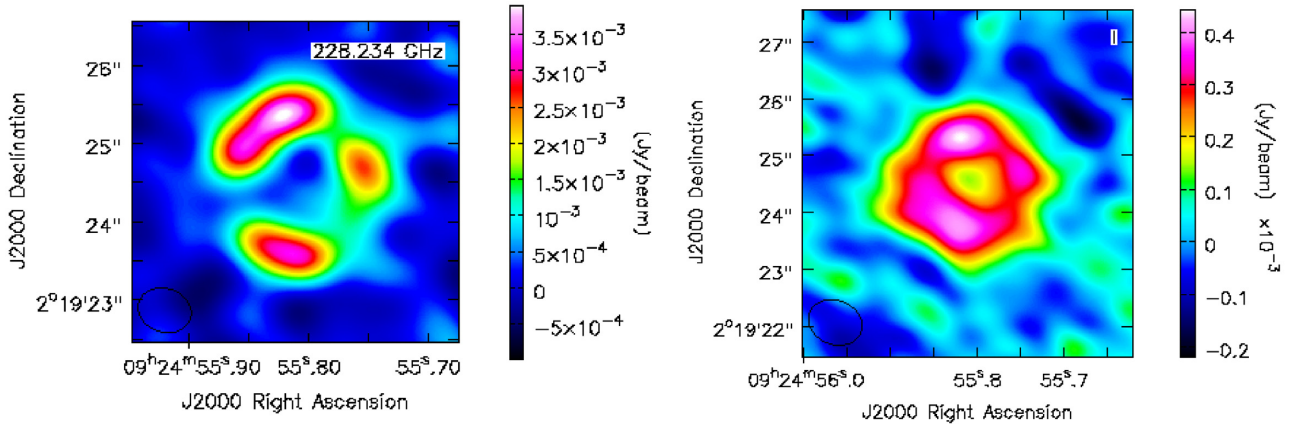

Figure 2. Left: The CO(5–4) integrated line emission with the continuum subtracted. This image was obtained using CLEAN in CASA with Briggs weighting, giving a resolution of 0.68 arcsec × 0.56 arcsec in PA 69.77°. The noise level in this map is 0.2 mJy beam^{-1}. The flux density is 21.99 ± 2.21 mJy, assuming a 10 per cent flux calibration accuracy. Right: Map of the submillimetre continuum obtained by cleaning the line-free spectral windows of the ALMA data with Briggs weighting. The flux density is 2.3 ± 0.2 mJy, assuming a 10 per cent flux calibration accuracy.

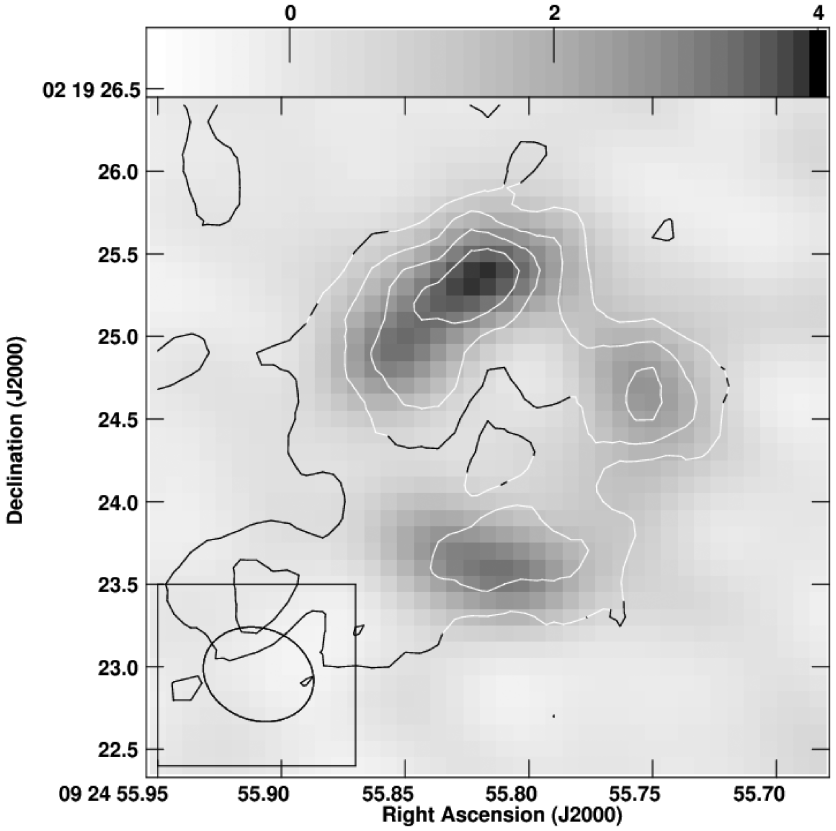

Figure 3. ALMA image (greyscale) of the integrated CO(5–4) emission with VLA radio contours overplotted. The greyscale runs from −1.0 to 4 mJy beam^{-1}, and the radio contours are given at (2, 4, 6, 8, 16, 32, 64, 128) times the rms noise level. The radio image has been convolved down to the ALMA beam.

Velocity-resolved maps of the CO line are shown in Fig. 5, and show clear velocity structure across the source, with parts of the source moving at different velocities being in different places in the source plane and thus producing different image configurations [also see Fig. 6 for the integrated CO(5–4) line spectrum]. The first-moment map (with the continuum subtracted from the CO line emission) showing the velocity structure across the lensed source and the second-moment map showing the velocity dispersion can be seen in Fig. 7.

3 ANALYSIS AND RESULTS

In the following sections, we describe the analysis of the ALMA CO(5–4) line image, the submillimetre continuum, and the VLA image. Our normal procedure is to obtain an initial model in the image plane, directly by fitting to the components of the image or using a lens model to fit a lensed source. This analysis is then used as a starting point for analysis of the data in the $u - v$ (Fourier) plane. This analysis is done either by fitting the image as separate

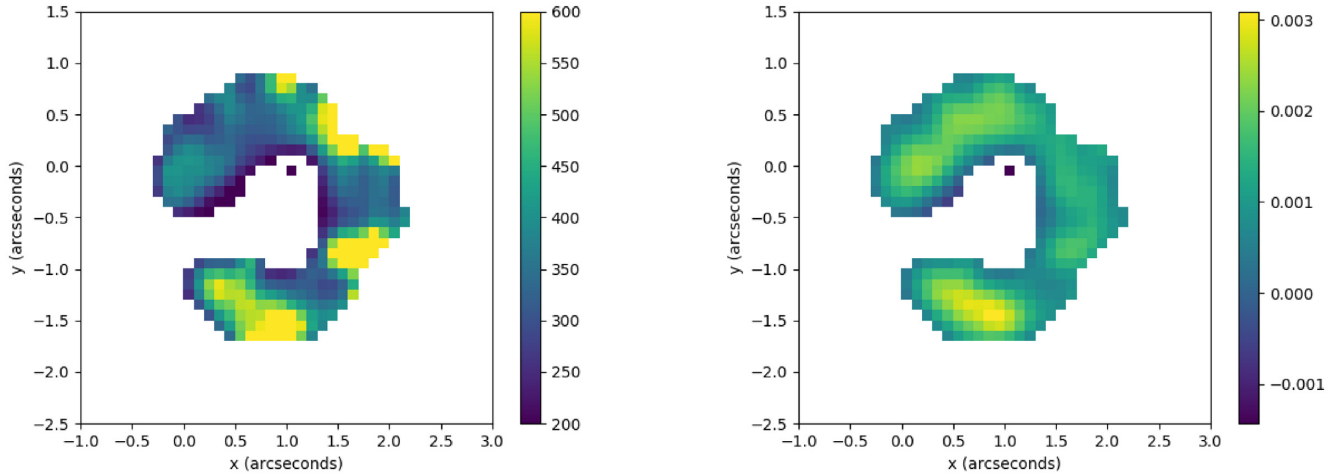

Figure 4. Left: Map of the CO line emission divided by the VLA map convolved down to the ALMA beam. The x and y values are in arcseconds. Right: Map showing the ALMA image (normalized) subtracted by the VLA image (normalized). The ALMA and the VLA images (convolved to the ALMA beam) were, each, normalized by dividing each of them by the total flux density in the images, as the order of the flux densities in the two images are different.

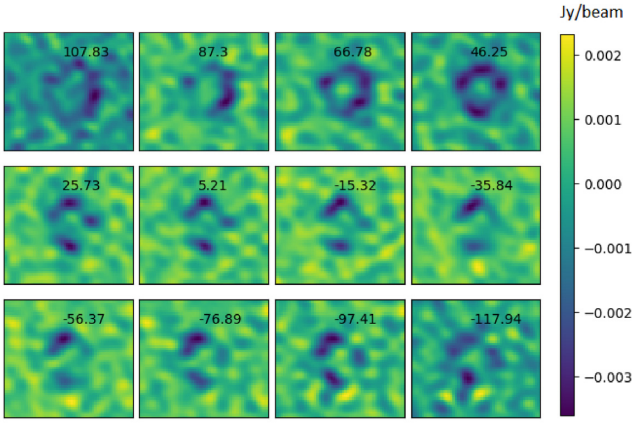

Figure 5. Slices through the ALMA CO(5–4) image cube at different frequencies; velocities on each plot are given in km s^{-1} with respect to a redshift of 1.5254, the centroid of the CO emission. The colourbar is in unit of Jy beam^{-1}.

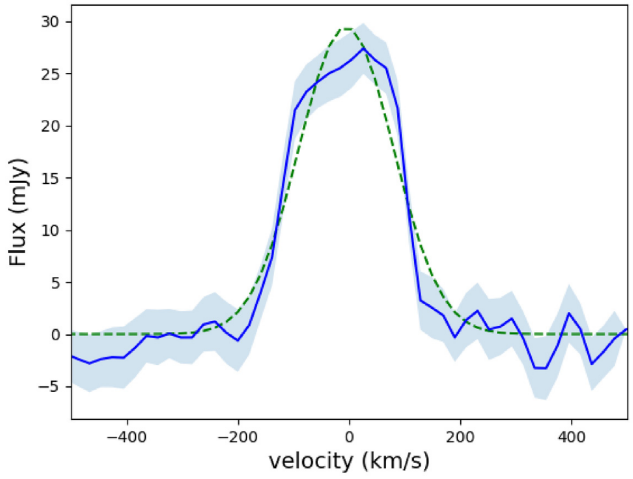

Figure 6. Integrated CO(5–4) line spectrum, with the velocity centre at $z = 1.5254$. The blue curve is the actual spectrum and the green dashed curve the Gaussian fit. The shaded light blue region represents the 1σ uncertainty on the spectrum.

components using UVMULTIFIT (Martí-Vidal et al. 2014) or using a lens model and the VISILENS package (Hezaveh et al. 2013b; Spilker et al. 2016) with a parametrized lensed source. We describe both phases of this process, first because the initial starting model is typically necessary to get good convergence in the $u - v$ fitting part of the process, and because it allows easy visual assessment of the fits.

3.1 ALMA observations: the molecular disc and submillimetre continuum

3.1.1 The integrated line emission

In the image plane, we began by fitting four elliptical Gaussians at the positions of the images in the CO(5–4) line map, an approach that makes no assumption about the detail of the lens model, in particular, its substructure content. The fit used 10 image parameters, namely the peak flux densities of the four components, the FWHMs and the axial ratios of images A and B and two overall positional offsets in the x and y directions respectively to allow for astrometric differences in the radio and optical images. The FWHMs and axial ratios of the merging images (A and D) are assumed equal, as are the FWHMs and axial ratios for images B and C, and the fitted components were constrained to have the major axes tangential to the centre of the lensing galaxy (100.87°, 77.21°, 12.99°, and 151.07° for A, B, C, and D, respectively; derived from positions of the images in Inada et al. (2003). Since the lensed images are spatially resolved, the FWHMs of the images were constrained to be greater than the major axis of the dirty beam. The 10-parameter optimization yielded a minimum $\chi^2_{\rm red} = 1.5$. The resulting lensed image and residual for this best fit is shown in Fig. 8(b) (bottom right). Table 3 (values in brackets) shows the parameters of the best-fitting model. The A/D flux ratio for this model was found to be 1.07. The modelled images B and C are clearly wider than would be expected in any plausible gravitational lens model.

In addition, we performed a gravitational lens modelling[3] using the singular isothermal ellipsoid (SIE) model developed by

[3]Throughout this study, we have used the lens modelling code developed by Neal Jackson.

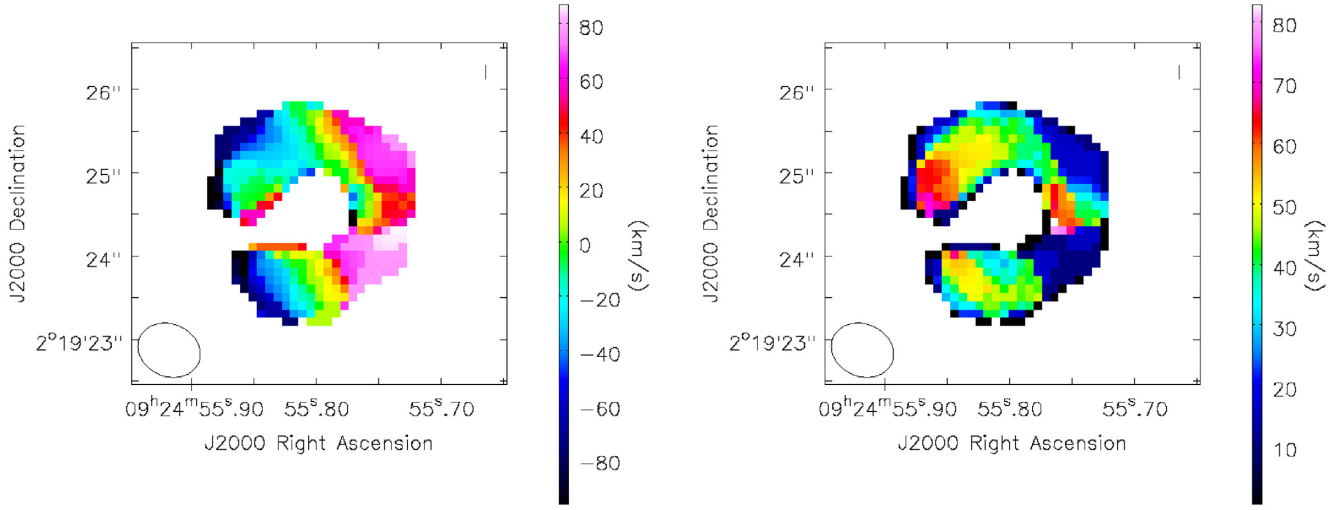

Figure 7. Left: ALMA first-moment map showing the velocity structure across the lensed images, with the velocities being with respect to the centroid of the line emission (found to be at 228.22 GHz, thus corresponding to a redshift of $z = 1.5254$). Right: Moment two map (velocity dispersion) of the continuum-free CO line emission. To obtain both these maps, we included only the pixels that have a signal to noise (off-source noise in the channel maps) ratio greater than 4.

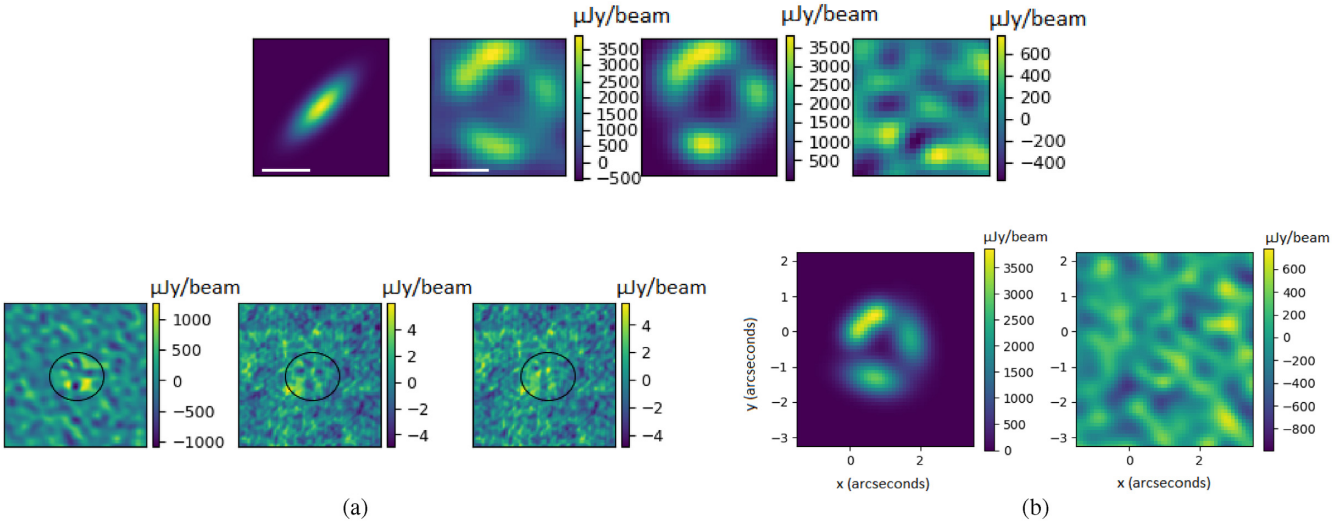

Figure 8. Image-plane fitting to ALMA CO line and radio images. Top: The best-fitting lensed image for the SIE lens model by Eigenbrod et al. (2006). The first image from the left is the source structure, the second the CO line image from the data, the third the lensed image and the fourth the corresponding residual map. The bars in the first and the second figures from the left represent 0.1 arcsec in the source figure and 1 arcsec in the lensed image, respectively. The flux density is in unit of μJy beam^{-1}. $\chi^2_{\rm red} = 1.85$. Bottom left (a): Residual maps corresponding to the best-fitting lens model for a point source, projecting to four PSF-sized lensed images (inside the oval region). From the left: residual for (1) CO line map, (2) radio map convolved to ALMA beam, and (3) radio map at its original resolution. It can be clearly seen that there is an oversubtraction of flux at the position of the images and undersubtraction in the nearby areas. The flux density units are in μJy beam^{-1}. Bottom right (b): Best-fitting CO-line lensed image and the corresponding residual map obtained by fitting four elliptical Gaussian components at the image positions ($\chi^2_{\rm red} = 1.5$). The A/D flux ratio for this best-fitting model was found to be 1.07. The unit of flux density in the image is μJy beam^{-1} and the x and y values are in arcseconds.

Eigenbrod et al. (2006) for the lensing galaxy. Allowing the source to have a Gaussian profile, the galaxy position and the source parameters were optimized using the difference between the data and the lensed images convolved with the point spread function. An extra parameter, $f_{\rm AD}$, was introduced, that can vary between 0 and 1 and which multiplies the flux of the component D, while keeping the flux of A the same. This parameter quantifies the anomaly in the flux ratio of A and D due to substructure effects, with a value of 1 indicating the situation of no flux anomaly present due to CDM substructure. Due to the relatively low signal-to-noise ratio of the data, we did not attempt to pixelize the source and use semilinear source reconstruction (Warren & Dye 2003). The best-fitting lensed image, source structure, and the corresponding residual map obtained from the optimization are shown in Fig. 8 (top). The fit has a $\chi^2_{\rm red} = 1.85$ and is generally satisfactory apart from some difference in the structure of image B. The parameters for this model are shown in Table 4 (values in brackets). The best-fitting position of the lensing galaxy from the optimization corresponds to RA = 09$^{\rm h}$24$^{\rm m}$55$^{\rm s}$.813 and Dec. = 02°19′24″.454 and has been used for all subsequent image-plane analysis, wherever required.

Table 3. Parameters corresponding to the best-fitting model to image components obtained by fitting elliptical gaussians to the observed lensed images, in the integrated CO(5–4) line and the radio. Refer to the text for the priors on the model. The reduced chi squared value before the re-scaling of the visibility weights in the algorithm are 4.68 and 11.24 for the CO line and the radio, respectively. The flux densities for the CO line and the radio data are in mJy and μJy, respectively. FWHMs are in arcseconds. Quantities derived from the initial image-plane fitting are given in brackets, in the case of the radio data for the radio image convolved to the ALMA resolution; other data are from UVMULTIFIT fitting to the $u - v$ data. The bottom table shows the positions of the four images with respect to the lensing galaxy. For the $u - v$ fit, the positions from Inada et al. (2003) were used and kept fixed. Positions in square brackets correspond to the best-fitting model in the image plane fits.

	Flux density		**FWHM**		**Axial ratio**	
	CO line	Radio	CO line	Radio	CO line	Radio
A	5.39 ± 0.30 (4.5)	16.71 ± 3.41 (16.8)	0.48 ± 0.07 (0.8)	0.32 ± 0.12 (0.80)	0.75 ± 0.19 (0.83)	0.69 ± 0.26 (0.9)
B	6.71 ± 0.36 (7.1)	12.18 ± 3.16 (13.2)	1.32 ± 0.07 (1.25)	0.32 ± 0.12 (0.79)	0.35 ± 0.04 (0.58)	0.69 ± 0.26 (1.0)
C	7.41 ± 0.41 (5.7)	13.55 ± 3.14 (14.1)	1.32 ± 0.07 (1.25)	0.32 ± 0.12 (0.80)	0.35 ± 0.04 (0.58)	0.69 ± 0.26 (1.0)
D	3.41 ± 0.26 (4.2)	13.06 ± 3.25 (13.5)	0.48 ± 0.07 (0.8)	0.32 ± 0.12 (0.79)	0.75 ± 0.19 (0.83)	0.69 ± 0.26 (0.9)

	Relative positions (to lensing galaxy) (x, y) (arcsec)	
	CO line	Radio
A	(−0.162, 0.847) [(−0.06, 0.8)]	(−0.162, 0.847) [(−0.09, 0.77)]
B	(−0.213, −0.944) [(−0.11, −0.98)]	(−0.213, −0.944) [(−0.15, −1.02)]
C	(0.789, 0.182) [(0.89, 0.14)]	(0.789, 0.182) [(0.85, 0.1)]
D	(−0.702, 0.388) [(−0.60, 0.35)]	(−0.702, 0.388) [(−0.63, 0.30)]

Table 4. Parameters of source structures inferred from fits assuming a lens model, corresponding to the best fit for the integrated CO line, submm continuum and radio map (convolved to ALMA resolution) of SDSS J0924+0219. These were fitted in the $u - v$ plane with a Sérsic profile source using VISILENS, and (figures in brackets) with a Gaussian profile source in the image plane. Δx_{S0} and Δy_{S0} are the positions of the source with respect to the lens, in arcseconds. All angles are east of north. A standard galaxy model (critical radius 0.87 arcsec, ellipticity 0.13 at PA −73.1°, shear magnitude 0.042 at PA 65.4°) is used for the image plane fitting. For the $u - v$ plane fitting, the lens parameters are the same as for the image plane, except for the Einstein radius (0.92 arcsec) which was obtained by optimizing for it in case of the CO line visibility data and subsequently kept fixed for the submillimetre continuum and radio $u - v$ fits. The image plane fit for the submillimetre continuum did not involve the f_{AD} parameter.

Parameters	**CO line**	**Submm continuum**	**Radio**
f_{AD}	1	NA	0.97
Δx_{S0} (arcsec)	− 0.037 ± 0.009 (−0.020)	− 0.050 ± 0.019 (−0.026)	− 0.037 ± 0.010 (−0.025)
Δy_{S0} (arcsec)	− 0.036 ± 0.010 (−0.022)	− 0.017 ± 0.026 (0.005)	− 0.044 ± 0.009 (−0.019)
Source flux density (mJy)	0.954 ± 0.057 (0.8)	0.225 ± 0.048 (0.1)	0.003 ± 0.002 (0.0023)
Source FWHM (arcsec)	0.081 ± 0.008 (0.045)	0.260 ± 0.071 (0.21)	0.120 ± 0.089 (0.052)
Source axial ratio	0.41 ± 0.10 (0.36)	0.866 ± 0.122 (0.92)	0.79 ± 0.17 (0.43)
Source PA (°)	223.85 ± 7.55 (136.0)	171.50 ± 131.07 (0.0)	162.16 ± 117.79 (125)
Sérsic index	0.5 ± 0.3	1.029 ± 0.489	1.784 ± 0.324

The value of f_{AD} for the best fit is 1. We also attempted to fit a lens model assuming a point source, giving unresolved point images[4]; the resultant residual shows an oversubtraction of flux in the image positions and undersubtraction in the nearby areas (see Fig. 8, bottom left), demonstrating incompatibility of a point source with our observation. The observation that $f_{AD} = 1$ implies that the SIE model we used clearly reproduces the main features of the data and is compatible with an extended source, together with no requirement for additional perturbations due to millilensing by substructure.

Given a starting model derived from the image plane, we now derived quantities directly from the $u - v$ data. We first fitted four elliptical Gaussians for the integrated CO line using UVMULTIFIT (Martí-Vidal et al. 2014), on the continuum-subtracted visibility data of the CO line. We used the positions of the four images from Inada et al. (2003) and kept them fixed, optimizing for the flux densities, widths, and axial ratios of the images. We kept the axial ratios of A and D (and likewise B and C) equal, as well as their FWHMs. The parameters corresponding to the best fit from the optimization can be found in Table 3. The flux ratio A/D obtained from this fitting was found to be 1.58 ± 0.15, which is slightly bigger than the corresponding flux ratio from the image plane analysis.

We also fitted the $u - v$ data with a lens model using VISILENS. All the lens galaxy parameters, except the position and mass of the lens galaxy, were fixed assuming the SIE lens model by Eigenbrod et al. (2006). We optimized for all the source parameters and the lens galaxy mass and position. Fig. 9 shows the best-fitting model and the residual map. The parameters for the best fit can be found in Table 4. The source FWHM using the $u - v$ plane analysis is 0.081 ± 0.008 arcsec, slightly larger than the FWHM found in the image plane analysis. Fig. 10 shows the distribution of the different parameters resulting from this lens model fitting.

We now proceed to calculate the luminosity of the CO(5–4) emission. Following Solomon & Vanden Bout (2005), we get a CO line (lensed) luminosity of $\mu L'_{CO} = 3.16 \times 10^{10}$ K km s^{-1} pc^2.

[4]The fit was performed using JMFIT, part of the Astronomical Image Processing System, AIPS, which is distributed by the US National Radio observatory, http://www.aips.nrao.edu.

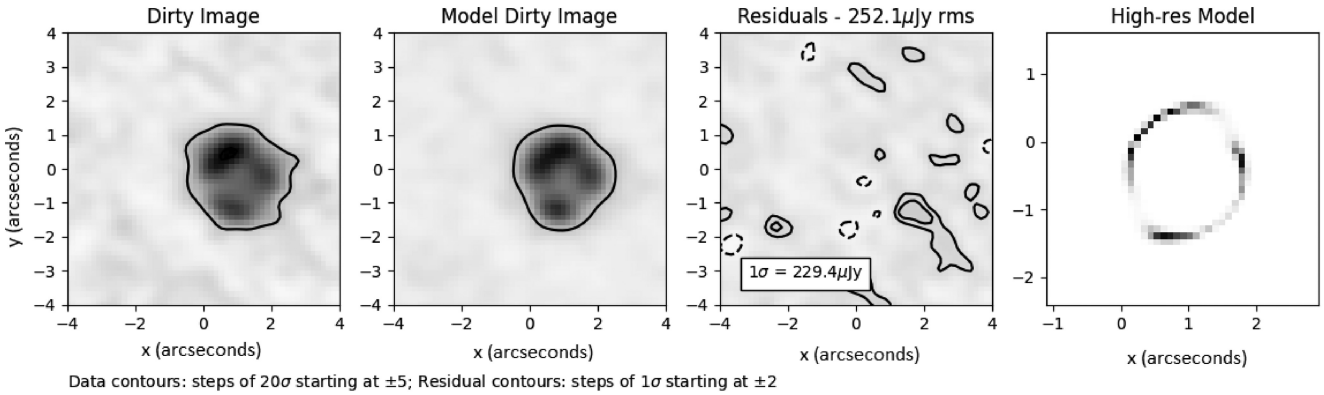

Figure 9. Best-fitting model obtained by fitting the Eigenbrod et al. (2006) SIE model to the visibility data of the CO(5–4) emission line, obtained using VISILENS.

The lens model fitting of the $u-v$ data using VISILENS demonstrates a source magnification of 23.5, making the intrinsic CO line luminosity equal to $L'_{\rm CO} \simeq 1.34 \times 10^9$ K km s^{-1} pc^2. Solomon & Vanden Bout (2005) use the formula $M_{\rm dyn}\sin^2(i) = 233.5R\Delta V^2$ to calculate the dynamical mass, where R is the radius of the molecular disc and ΔV is the FWHM of the CO line. Using our value of size of the integrated CO line emission source of 81 ± 8 mas (Table 4), we get $R = 348 \pm 34$ pc, approximating R to be equal to half of size of the disc. The FWHM of the line is 200 ± 7 km s^{-1}, thus giving a dynamical mass $M_{\rm dyn} = 3.25 \times 10^9 {\rm cosec}^2(i) {\rm M}_\odot$, where i is the inclination angle of the disc.

3.1.2 ALMA observations: velocity-resolved structure in the CO(5–4) line

The ALMA CO(5–4) line observations (Fig. 5) clearly show that the line originates in a structure with ordered spatial differentiation in velocity, such as rotation or possibly outflow. We can use a simple lens model to project the frequency planes of the ALMA data back into the source plane and thus determine simple parameters, such as size and rotation velocity of the emitting structure. The relatively low resolution of the ALMA observations does not allow us to ask more than simple questions of the data. In particular, we cannot derive the structure of the source in detail, nor do we have the sensitivity at high resolution needed for investigation of detailed structure within the mass model. Observations of another CO line which do allow this are presented in Stacey et al. (in preparation).

The relatively low resolution, and the complexity of the information about the source that we seek, motivate a simple analysis in which we project each of the frequency-sliced images back to the source plane, without modelling the $u-v$ data explicitly. This was the approach taken using simple VLA information on the source HS 0810+2554 (Jackson et al. 2015) which proved to yield roughly correct values for the source size when higher quality observations became available (Hartley et al. 2019). We use the previous SIE lens model (Section 3.1.1) that allows us to fix the galaxy mass parameters, and we represent the source structure in each frequency plane as a single elliptical Gaussian, whose position, flux, width, axial ratio, and position angle we allow to vary in order to fit the data. The resulting source positions occupy a roughly linear configuration, with a clear sequence from red to blue across the frequency band. These assumptions about the source effectively constitute a regularization, which prevents the source structure from varying catastrophically as the model attempts to fit noise in the image.

The resulting source model, with the astroid caustic of the galaxy overlaid on top, is shown in Fig. 11. This caustic separates regions in which the source is doubly and quadruply imaged, and is a locus of infinite magnification. The source model in Fig. 11 is compatible with the images of the different CO planes in Fig. 5, and its position angle and ellipticity are compatible with the source structure inferred by modelling the integrated CO image. However, the interpretation of details in Fig. 11 has to be done with caution: while we may be tempted to interpret the source to be a warped disc, it should be noted that there could be a large error bar on the fit to the velocity planes towards the red end because of their low signal to noise, as can be seen from Fig. 5. Given the limited angular resolution, the structure could be consistent with a rotating molecular disc (e.g. Smit et al. 2018), which has a size of between 0.1 and 0.3 arcsec depending on the exact centroids inferred for the lower-frequency parts of the source, corresponding to ∼850–2500 pc at the redshift of this quasar. However, observations at higher angular resolution and sensitivity are required to confirm this hypothesis. The size of the structure, and the overall distribution of velocities, is robust to different assumptions about the source structure, such as allowing the source components corresponding to each frequency plane to be circular Gaussians.

3.1.3 The submillimetre continuum

Fig. 2 shows that the lensed submillimetre continuum displays a ring structure, but which appears subtly different in the distribution of bright features to the CO line image. A simple lens model of this structure, using the same SIE galaxy lens model as before, gives a best fit in which the continuum source is somewhat offset from the line; the best-fitting source position is indicated in Fig. 11. It appears closer to the northeastern fold caustic, in agreement with the appearance of the lensed continuum map which suggests a different position for the merging image in the continuum and line maps. This result requires confirmation, however, with a longer observation. The source structure, lensed image configuration, and the residual map obtained using the SIE galaxy lens model are shown in Fig. 12; the width of the continuum source from the model is about 0.21 arcsec (≈1.8 kpc at the redshift of this source). This is found to be more compact compared to the dust emission from a sample of dusty star-forming galaxies studied by Hodge et al. (2016, 2019).

The source parameters from this image-plane fit were used as initial parameters to perform a $u-v$ plane fitting using VISILENS,

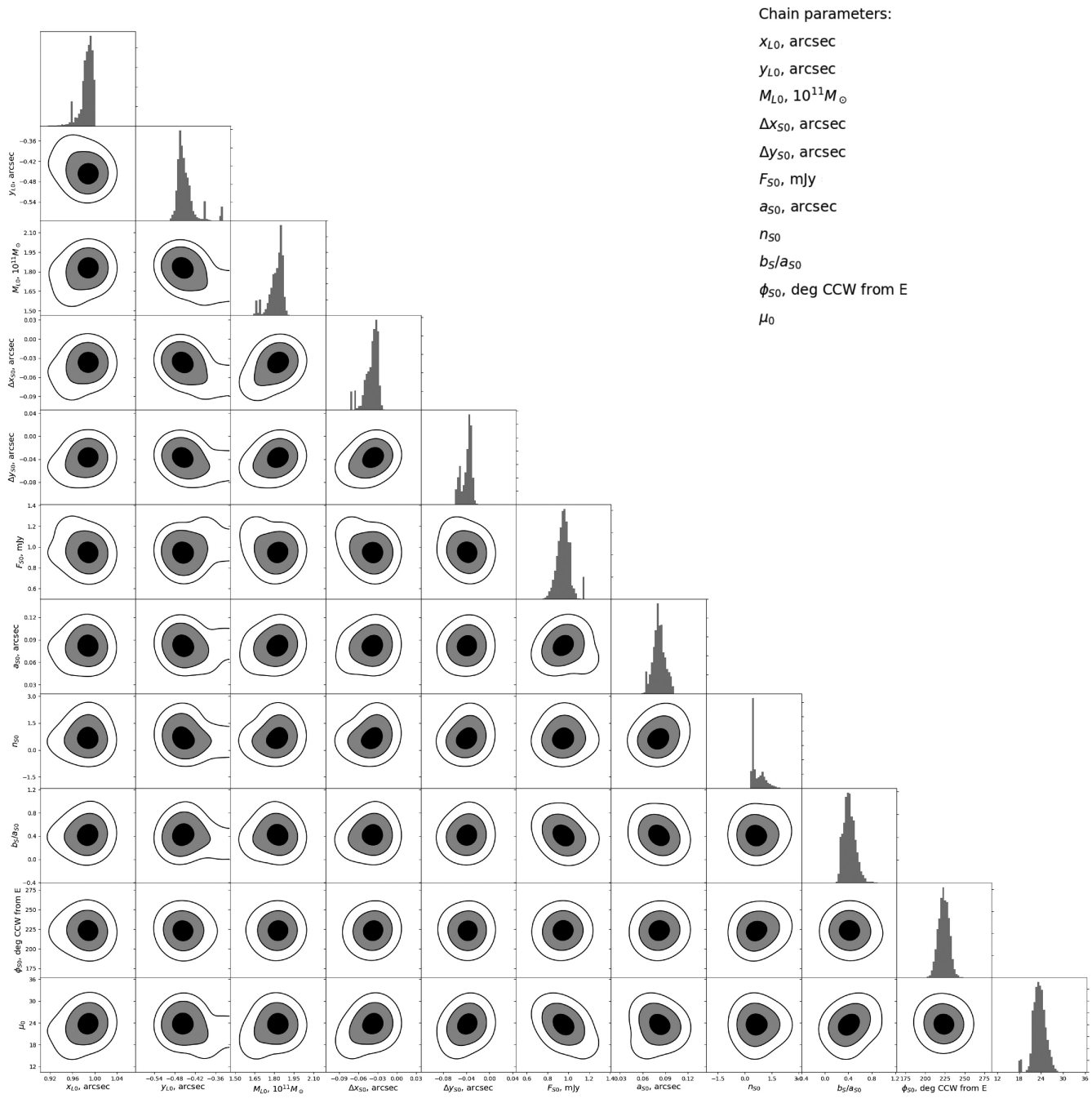

Figure 10. Corner plot showing the distribution for different parameters, obtained by fitting a lens model to the CO(5–4) visibility data using VISILENS, described in Section 3.1.1. For this optimization, all lens galaxy parameters were kept fixed, except the lens galaxy mass and position. We also optimized for all source parameters. The parameters (with their units) are shown in the upper right corner for clarity. They refer to position of lensing galaxy, mass of the lensing galaxy, position of source with respect to the lensing galaxy, flux of the CO source, width of the source, Sersic index, source axial ratio, phase angle, and magnification.

incorporating the SIE model of Eigenbrod et al. (2006). For the optimization, we kept the parameters of the lensing galaxy fixed (using the lensing galaxy position and mass derived from the optimization of the CO line visibility data using VISILENS previously) and let the source parameters vary. We assumed the source to have a Sérsic profile (Fig. 12). The size of the submillimetre continuum found using $u - v$ plane fitting (0.26 ± 0.07 arcsec, Table 4) is consistent with the size of 0.21 arcsec found using the image plane fitting.

3.2 Radio

In the VLA map of SDSS J0924+0219 (Fig. 1), we detect all four lensed images in the system, and it is clear that the ratio of the fluxes in the A and D images is less than the value of 12 that is measured in the optical waveband, but that the flux densities of the two images do not look equal. We again began by fitting Gaussian components in the image plane. A preliminary fit of the four lensed images with point-like Gaussian components, using AIPS JMFIT, gave obviously

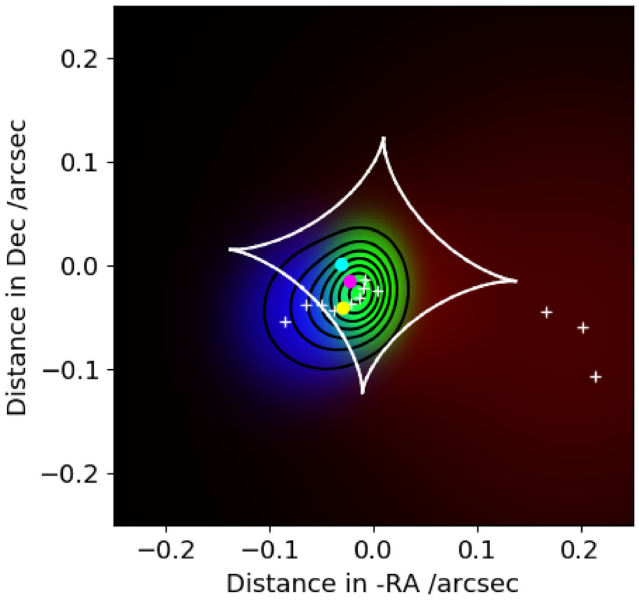

Figure 11. Reconstructed source based on the ALMA observations, coloured according to frequency of the source (see text). The astroid caustic of the model galaxy is overlaid. The white crosses are the positions of the sources for the individual CO planes. The black contours are the sum of contours of the sources in all the planes. The circles in yellow and magenta correspond to the position of the optical and the radio source, respectively. The circle in cyan corresponds to the submillimetre continuum source (refer to Fig. 12).

unsatisfactory results, similar to what is seen for the CO line map (Fig. 8). This shows that the radio source is also extended.

The flux ratio of components A and D was determined using the radio map, convolved to the ALMA beam size, using the Gaussian fitting method described earlier for the CO line, with the same 10 image parameters. The best fit, of $\chi^2_{\rm red} = 1.8$, yielded an A/D flux ratio of 1.25; on the original map we obtained 1.28. The best-fitting model and its parameters are shown in Fig. 13 and Table 3 (values in brackets). For illustration, Fig. 13 shows what the lensed image and the corresponding residual would look like if we constrained the A/D flux ratio for this lens model to be 12, the ratio observed in the optical waveband. It confirms our previous result that the radio data do not demonstrate an A/D flux ratio of 12 and is more consistent with a lower flux ratio. We carried out the lens modelling of the radio image, convolved to the ALMA beam and incorporating the same SIE model for the lensing galaxy as we did for the ALMA data (Section 3.1.1) and assuming a Gaussian function for the source structure. We kept the lensing galaxy parameters fixed and optimized only for the source and the $f_{\rm AD}$ parameter. The source structure, the best fit lensed image and the residual map corresponding to the lens model ($\chi^2_{\rm red} = 2.05$) are shown in Fig. 13 and the corresponding parameters in Table 4 (values in brackets). Similar to the CO line image, the $f_{\rm AD}$ parameter in this case is also close to 1, implying that any flux anomaly in the radio can be attributed to the extended source structure.

These image-plane fits were used to start the fitting in the $u - v$ plane. As for the integrated CO line, we fitted four elliptical Gaussians to the visibility data using UVMULTIFIT, with image positions from Inada et al. (2003) and fixing the component position angles. The four image flux densities, FWHMs, and axial ratios were optimized, keeping the FWHMs and axial ratios of the four images equal, because using any more parameters than these six (four flux densities, one width, and one axial ratio) resulted in the programme failing to find a fit. The parameters for the best-fitting model are tabulated in Table 3. The flux ratio A/D obtained from this fitting was found to be 1.28 ± 0.41, once again consistent with the flux ratio found from the image-plane analysis.

Following the same approach as for the CO(5–4) line, we fixed the lens galaxy parameters and optimized for the source parameters in VISILENS. Fig. 13 shows the best-fitting model and the residual map and Table 4 shows the corresponding parameters. Even though the median size of the radio source inferred from the $u - v$ fit is seen to be only 1.3σ away from zero, it can be seen from Fig. 8 that the radio data are inconsistent with a point source. We also find that the radio source size is sensitive to the starting parameters of the $u - v$ fit optimization.

4 DISCUSSION AND CONCLUSIONS

There are two interesting questions we can attempt to answer with these data, the answer to the second of which is related to the first:

(i) What is the size of the radio-emitting region, what physical processes produce it, and is it co-spatial with the molecular line gas?

(ii) Is the optical flux anomaly due to microlensing?

We discuss these two points in the following sections.

4.1 The radio source and the CO(5–4) line

Although we do not have the resolution to study the structure of the molecular disc in detail, it appears from the ALMA CO(5–4) observation that we could be seeing a structure in ordered motion, the natural explanation of which is the presence of a rotating molecular disc. The structure is of physical dimension approximately 100–300 mas (∼850–2500 pc), consistent with a compact star-forming disc in the centre of the host galaxy of SDSS 0924+0219. We have performed simple modelling of the radio data (which is all that is warranted given the signal-to-noise and resolution of the data) and derive inconsistency with a point source, and a preferred size of about 100 mas, consistent with the size of the CO-line source. From Fig. 3, we see that the lensed structures in the radio and CO lines are consistent with each other. Although not conclusive, the most natural explanation is therefore that the two components of the source originate from a region that is of the same size and physical origin. Combining the radio flux density from this work with the previously determined far-IR flux densities of Stacey et al. (2018), it appears that SDSS J0924+0219 lies on the standard radio–FIR correlation (Ivison et al. 2010); the corresponding $q_{\rm IR}$ parameter is found to be 2.35, well within the range of $q_{\rm IR} = 2.40 \pm 0.24$ found by Ivison et al. (2010). Thus the conclusion of radio emission produced in a star-forming region appears natural. The physical size of the disc, of order of a kiloparsec, is similar to, or slightly smaller than that found in other high-redshift lensed quasars with mid-*J* CO transition (Alloin et al. 1997; Downes et al. 1999; Venturini & Solomon 2003; Anh et al. 2013; Rybak et al. 2015; Geach et al. 2018). It is also found to be similar or more compact in size to mid-*J* transition CO emission regions in high-redshift, unlensed quasars (Beelen et al. 2004; Riechers et al. 2009b; Polletta et al. 2011; Brusa et al. 2018; Feruglio et al. 2018). The unlensed flux density of the CO line and the molecular gas mass are both about a factor of 10 smaller than those of the radio-loud quasars JVAS B1938+666 and MG 0751+2716 (Spingola et al. 2019), although the observations

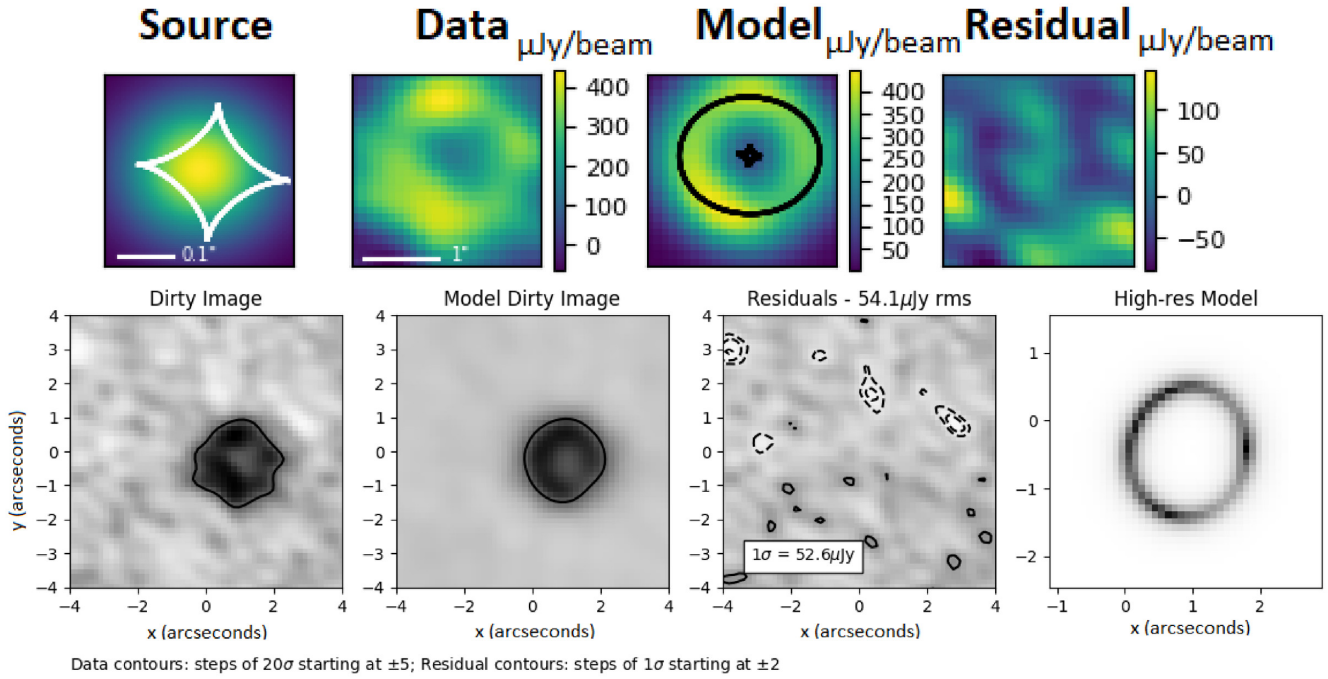

Figure 12. Top, left to right: The best-fitting source structure, data, lensed image configuration, and residual map obtained from the image-plane lens modelling of the submillimetre continuum using the SIE galaxy lens model (Eigenbrod et al. 2006) used in Section 3.1.1 ($\chi^2_{\rm red} = 1.19$). The bars in the first and the second figures from the left represent 0.1 arcsec in the source figure and 1 arcsec in the lensed image, respectively. The flux density is in units of μJy beam^{-1}. The curves in the source and the model panels show the astroid caustic and the critical curve. Bottom: Fit to the $u - v$ data of the submm continuum, starting with the image-plane fit.

are not strictly comparable as the higher order CO line in this investigation preferentially traces warmer gas, which tends to be more compact than the cold molecular gas. Fig. 14 shows the spectral energy distribution (SED) of SDSS J0924+0219, based on this work and previous studies carried out by Stacey et al. (2018) and Jackson et al. (2015). The SED was found to correspond to a dust temperature of $T = 30.8 \pm 0.8$ K and emissivity index $\beta = 1.6 \pm 0.08$.

Our ALMA observations detect the submillimetre continuum source, although at a relatively low signal-to-noise level. Modelling of these observations gives a preliminary indication that the submillimetre continuum source, which traces the illuminated dust, may be spatially displaced from the region emitting the molecular line and radio emission, although this requires confirmation from deeper observations. Whether the radio emission contains partial contribution from an AGN-type source, as in HS 0810+2554 (Hartley et al. 2019) will be interesting to determine from future VLBI observations. The submillimetre source is also more extended than the CO emitting region; it may be that star formation is taking place in only part of the overall structure of dust and gas at the centre of the object.

4.2 Is microlensing the reason behind the optical flux ratio anomaly?

We now turn to the second question concerning the optical flux ratio anomaly. In the case of SDSS J0924+0219, the flux ratio between the brightest image and its merging counterpart in the radio was robustly determined as 1.28 ± 0.41, consistent with all methods of analysis. Similar results are obtained from the CO line images, and at this resolution the observations are consistent with a combination of a smooth lens model and an extended source. Fig. 15 shows the variation in flux ratio in SDSS J0924+0219 with wavelength.

These results are consistent with the theory that the optical flux anomaly can be attributed to microlensing, a conclusion that is also consistent with previous studies of this object (Keeton et al. 2006; Morgan et al. 2006). As mentioned earlier, 15 yr seems to be a long time for microlensing to persist. To test that such a long period of demagnification is plausible, we simulated a microlensing magnification map corresponding to image D using the ray-tracing tree code developed by Wambsganss (2001). We built a map with 100 microlensing Einstein radius η_0 side-length and 0.005 η_0 / pixel resolution. For SDSS J0924+0219, Mosquera & Kochanek (2011) calculate $\eta_0 \sim 3.2 \times 10^{16}$ cm for an average microlens mass $\langle M/{\rm M}_\odot \rangle = 0.3$, and a transverse velocity of $v_{\rm trans} = 0.049\,\eta_0$/yr. We use convergence and shear values at the position of image D as derived by Keeton et al. (2006) [i.e. $(\kappa, \gamma) = (0.48, 0.57)$], a fraction of surface density in form of stars of $\alpha = 0.07$. This value of dark matter fraction is at the low side of values derived from microlensing at a projected distance of $\sim$1 Einstein radius from the lens centre (Jiménez-Vicente et al. 2015). To account for the optical-source size, we convolve the map by a Gaussian profile with half-light radius $R_{1/2} = 0.02\eta_0$, corresponding to the I-band magnitude accretion disc source size expected in the framework of the standard accretion disc model (Mosquera & Kochanek 2011). Fig. 16 shows a fraction of this map where multiple regions demagnified by at least a factor 12 are observed. Those regions extend over several η_0, which translates to periods of demagnification that can last over 20–60 yr. This result remains qualitatively unchanged if we increase the source size by a factor of 3, to account for the fact the optical continuum emission may be larger than expected by the standard model of accretion (Morgan et al. 2010; Edelson et al. 2015; Hutsemékers, Sluse & Kumar 2020).

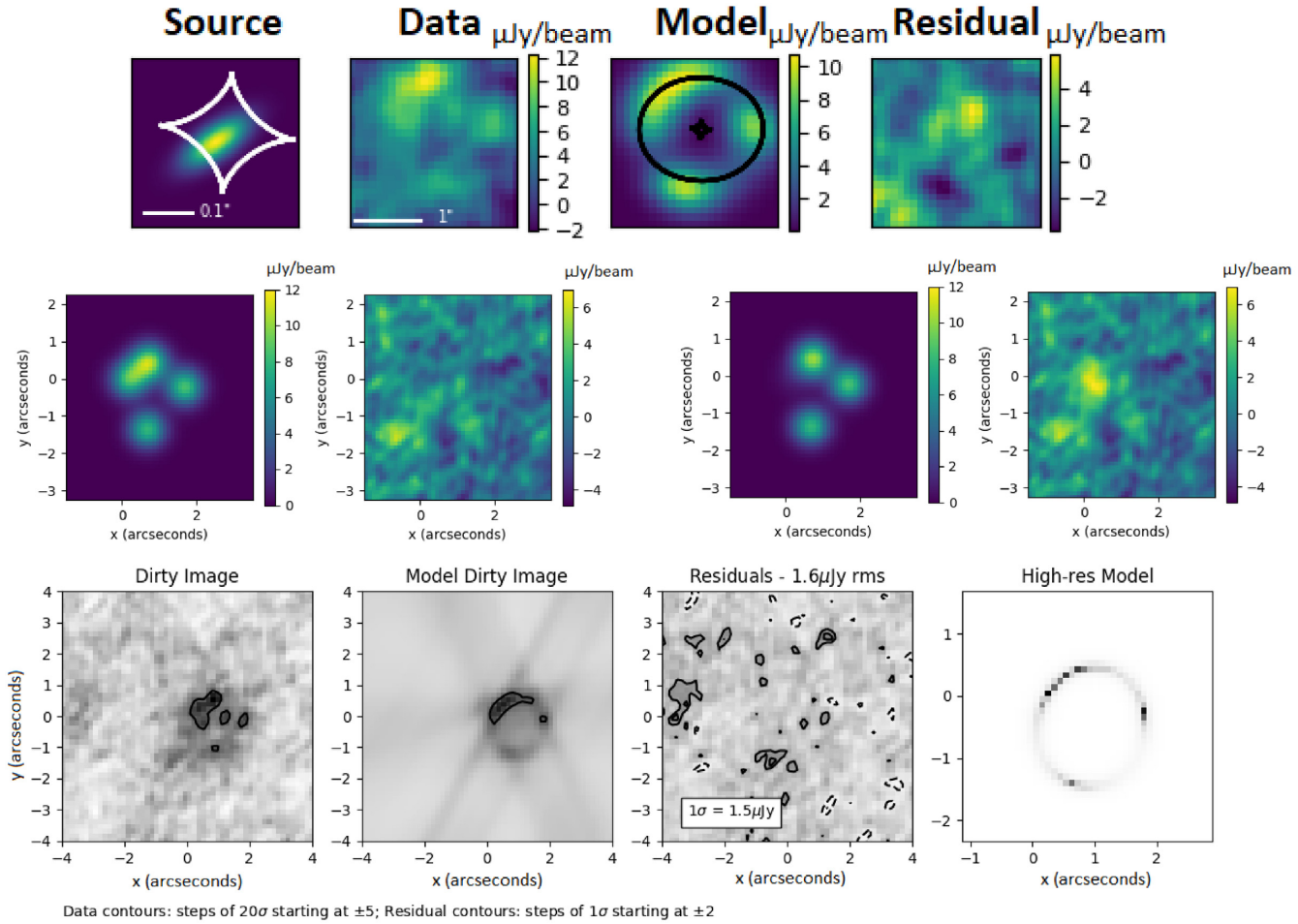

Figure 13. Top: The best-fitting image-plane lens model for the radio map (convolved to the ALMA beam) assuming the SIE lens model by Eigenbrod et al. (2006) ($\chi^2_{\rm red} = 2.05$). The bars in the first and second figures from the left represent 0.1 arcsec in the source figure and 1 arcsec in the lensed image, respectively. The flux density is in units of μJy beam^{-1}. The curves in the source and the model panels show the astroid caustic and the critical curve. Middle: (Left) Image plane fit with elliptical Gaussian components, with residual: (Right) the same, but enforcing a 12:1 ratio between components A and D. Bottom: Image, model, residual and high-resolution model from the $u - v$ plane fit.

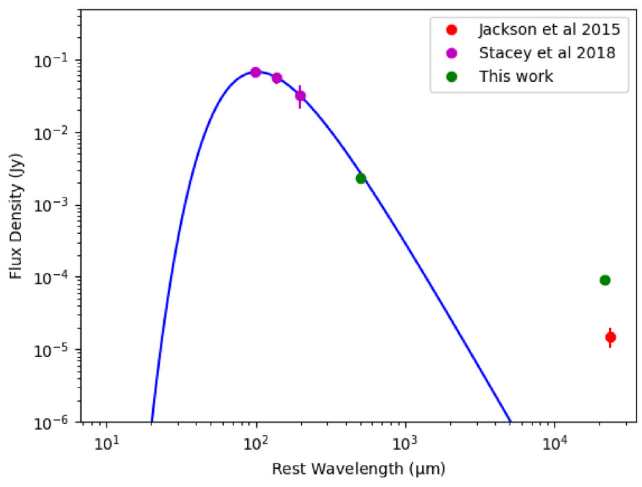

Figure 14. The spectral energy distribution of SDSS J0924+0219, corresponding to a dust temperature of $T = 30.8 \pm 0.8$ K and $\beta = 1.6 \pm 0.08$. The SED was fit to the modified blackbody curve defined by $S_\nu \propto \frac{\nu^{3+\beta}}{e^{\frac{h\nu}{kT}} - 1}$, where h is the Planck constant, k the Boltzmann constant, β the emissivity index, and T the dust temperature.

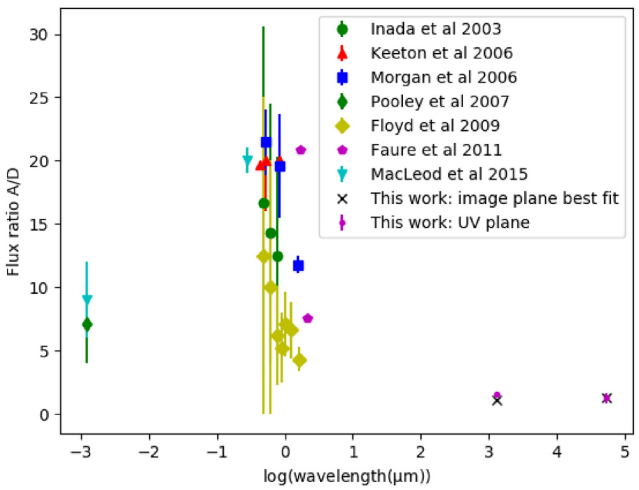

Figure 15. Flux ratios in SDSS J0924+0219 over different wavelengths. The data for this plot have been taken from table 2 in Floyd, Bate & Webster (2009), Keeton et al. (2006), Morgan et al. (2006), Faure et al. (2011), and MacLeod et al. (2015). The logarithm in the x-axis is in base 10.

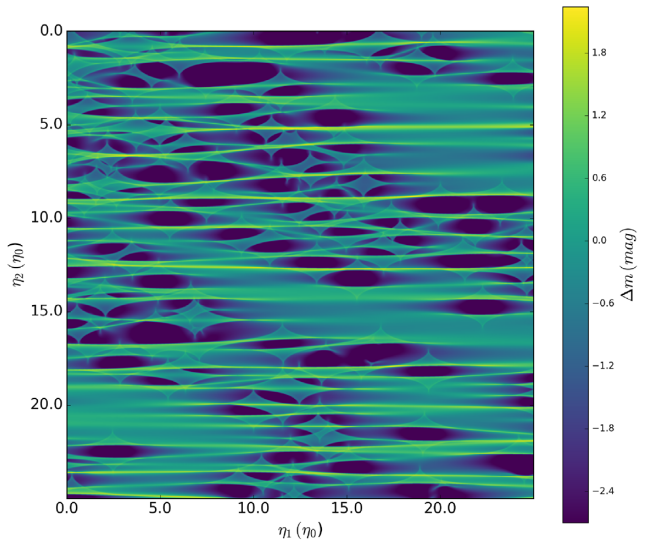

Figure 16. Microlensing magnification map associated with image D. We zoom over a region of 50 × 50 η_0. The colour scale corresponds to the micro(de)magnification of a Gaussian source of half-light radius $R_{1/2} = 0.06$ η_0 ($=1.8 \times 10^{15}$ cm $= 5.8 \times 10^{-4}$ pc). By convention, micro-magnification $\Delta m > 0$ corresponds to the bright regions, and demagnification corresponds to $\Delta m < 0$ as indicated by the colourbar. Several regions with demagnification stronger than $|\Delta m| = 2.7$ mag (i.e. corresponding to a flux ratio 1:12 as observed in image *D* over the last decade) are detected. Those regions sometimes extend over several microlensing Einstein radii η_0.

The overall importance of observing systems like SDSS J0924+0219 is that such observations contribute to the slow increase in the number of four-image strong lenses with available fluxes at optical wavelengths as well as wavelengths where the sources are large enough to be immune to microlensing. Xu et al. (2015) considered the then best available sample of radio lenses and studied the effect of CDM substructure on each lens of the sample by adding substructure using Aquarius and Phoenix simulations to the macro models of the lens and examining the resulting flux ratio distributions, but like their predecessors was limited to the then available sample of ∼10 systems. The joint analysis of radio studies of radio-quiet quasars and submillimetre/extended emission-line studies is likely to be useful in investigating the physics of the radio emission and its relation to the molecular gas component (and possibly also substructure, with availability of the higher resolution submillimetre data).

ACKNOWLEDGEMENTS

The Karl G. Jansky Very Large Array is operated by the US National Radio Astronomy Observatory. NRAO is a facility of the National Science Foundation operated under cooperative agreement by Associated Universities, Inc. This paper makes use of the following ALMA data: ADS/JAO.ALMA2018.1.01447.S. ALMA is a partnership of ESO (representing its member states), NSF (USA), and NINS (Japan), together with NRC (Canada), MOST and ASIAA (Taiwan), and KASI (Republic of Korea), in cooperation with the Republic of Chile. The Joint ALMA Observatory is operated by ESO, AUI/NRAO, and NAOJ. The authors would like to thank Ian Browne and an anonymous referee for their comments on the paper, Justin Spilker for his help with VISILENS and George Bendo for his assistance with the ALMA data analysis.

REFERENCES

Alloin D., Guilloteau S., Barvainis R., Antonucci R., Tacconi L., 1997, A&A, 321, 24
Amara A., Metcalf R. B., Cox T. J., Ostriker J. P., 2006, MNRAS, 367, 1367
Anh P. T., Boone F., Hoai D. T., Nhung P. T., Weiß A., Kneib J.-P., Beelen A., Salomé P., 2013, A&A, 552, L12
Aravena M. et al., 2016, MNRAS, 457, 4406
Atek H. et al., 2015, ApJ, 800, 18
Beelen A. et al., 2004, A&A, 423, 441
Bonzini M. et al., 2015, MNRAS, 453, 1079
Brusa M. et al., 2018, A&A, 612, A29
Burud I. et al., 2002, A&A, 383, 71
Chang K., Refsdal S., 1979, Nature, 282, 561
Chiba M., 2002, ApJ, 565, 17
Chiba M., Minezaki T., Kashikawa N., Kataza H., Inoue K. T., 2005, ApJ, 627, 53
Condon J. J., Kellermann K. I., Kimball A. E., Ivezić Ž., Perley R. A., 2013, ApJ, 768, 37
Croton D. J. et al., 2006, MNRAS, 365, 11
Dalal N., Kochanek C. S., 2002, ApJ, 572, 25
Deane R. P., Heywood I., Rawlings S., Marshall P. J., 2013, MNRAS, 434, 23
Downes D., Neri R., Wiklind T., Wilner D. J., Shaver P. A., 1999, ApJ, 513, L1
Edelson R. et al., 2015, ApJ, 806, 129
Eigenbrod A., Courbin F., Dye S., Meylan G., Sluse D., Vuissoz C., Magain P., 2006, A&A, 451, 747
Fadely R., Keeton C. R., 2011, AJ, 141, 101
Fadely R., Keeton C. R., 2012, MNRAS, 419, 936
Fassnacht C. D. et al., 1998, AJ, 117, 658
Faure C., Sluse D., Cantale N., Tewes M., Courbin F., Durrer P., Meylan G., 2011, A&A, 536, A29
Feruglio C. et al., 2018, A&A, 619, A39
Floyd D. J., Bate N. F., Webster R. L., 2009, MNRAS, 398, 233
Gaia Collaboration, 2018, A&A, 616, A1
Geach J. E., Ivison R. J., Dye S., Oteo I., 2018, ApJ, 866, L12
Gilman D., Birrer S., Treu T., Nierenberg A., Benson A., 2019, MNRAS, 487, 5721
Hartley P., Jackson N., Sluse D., Stacey H. R., Vives-Arias H., 2019, MNRAS, 485, 3009
Herrera Ruiz N., Middelberg E., Norris R. P., Maini A., 2016, A&A, 589, L2
Hezaveh Y., Dalal N., Holder G., Kuhlen M., Marrone D., Murray N., Vieira J., 2013a, ApJ, 767, 9
Hezaveh Y. D. et al., 2013b, ApJ, 767, 132
Hezaveh Y. D. et al., 2016, ApJ, 823, 37
Hodge J. A. et al., 2016, ApJ, 833, 103
Hodge J. A. et al., 2019, ApJ, 876, 130
Hsueh J. W., Fassnacht C. D., Vegetti S., McKean J. P., Spingola C., Auger M. W., Koopmans L. V., Lagattuta D. J., 2016, MNRAS, 463, L51
Hutsemékers D., Sluse D., Kumar P., 2020, A&A, 633, A101
Högbom J. A., 1974, A&AS, 15, 417
Inada N. et al., 2003, AJ, 126, 666
Irwin M. J., Webster R. L., Hewett P. C., Corrigan R. T., Jedrzejewski R. I., 1989, AJ, 98, 1989
Ivison R. J. et al., 2010, A&A, 518, 1
Jackson N., 2011, ApJ, 739, L28
Jackson N., Tagore A. S., Roberts C., Sluse D., Stacey H., Vives-Arias H., Wucknitz O., Volino F., 2015, MNRAS, 454, 287
Jarvis M. E. et al., 2019, MNRAS, 485, 2710
Jiménez-Vicente J., Mediavilla E., Kochanek C. S., Muñoz J. A., 2015, ApJ, 799, 149
Keeton C. R., Burles S., Schechter P. L., Wambsganss J., 2006, ApJ, 639, 1
Kratzer R. M., Richards G. T., Goldberg D. M., Oguri M., Kochanek C. S., Hodge J. A., Becker R. H., Inada N., 2011, ApJ, 728, L18
MacLeod C. L. et al., 2015, ApJ, 806, 258
Maiolino R. et al., 2017, Nature, 544, 202

Mao S., Schneider P., 1998, MNRAS, 295, 587
Martí-Vidal I., Vlemmings W. H., Muller S., Casey S., 2014, A&A, 563, A136
Mcmullin J. P., Waters B., Schiebel D., Young W., Golap K., 2007, in Shaw R. A., Hill F., Bell D. J., eds, ASP Conf. Ser. Vol. 376, Astronomical Data Analysis Software and Systems XVI. Astron. Soc. Pac., San Francisco, p. 127
Metcalf R. B., Madau P., 2001, ApJ, 563, 9
Metcalf R. B., Zhao H., 2002, ApJ, 567, L5
Miranda M., Macciò A. V., 2007, MNRAS, 382, 1225
Morgan C. W., Kochanek C. S., Morgan N. D., Falco E. E., 2006, ApJ, 647, 874
Morgan C. W., Kochanek C. S., Morgan N. D., Falco E. E., 2010, ApJ, 712, 1129
Mosquera A. M., Kochanek C. S., 2011, ApJ, 738, 96
Moustakas L. A., Metcalf R. B., 2003, MNRAS, 339, 607
Möller O., Hewett P., Blain A. W., 2003, MNRAS, 345, 1
Nierenberg A. M. et al., 2017, MNRAS, 471, 2224
Nierenberg A. M. et al., 2020, MNRAS, 492, 5314
Padovani P. et al., 2017, A&AR, 25, 2
Paraficz D. et al., 2018, A&A, 613, A34
Peeples M. S., Schechter P. L., Wambsganss J. K., 2004, BAAS, 36, 1392
Poindexter S., Morgan N., Kochanek C. S., 2008, ApJ, 673, 34
Polletta M., Nesvadba N. P., Neri R., Omont A., Berta S., Bergeron J., 2011, A&A, 533, A20
Riechers D. A., Walter F., Carilli C. L., Lewis G. F., 2009a, ApJ, 690, 463
Riechers D. A. et al., 2009b, ApJ, 703, 1338
Riechers D. A. et al., 2011, ApJ, 739, L32
Rybak M., Vegetti S., McKean J. P., Andreani P., White S. D. M., 2015, MNRAS, 453, L26
Saha P., Williams L. L. R., Ferreras I., 2007, ApJ, 663, 29
Smit R. et al., 2018, Nature, 553, 178
Solomon P. M., Vanden Bout P. A., 2005, ARA&A, 43, 677
Spilker J. S. et al., 2016, ApJ, 826, 112
Spingola C. et al., 2020, MNRAS, 495, 2387
Stacey H. R. et al., 2018, MNRAS, 476, 5075
Stacey H. R. et al., 2019, A&A, 622, A18
Sugai H., Kawai A., Shimono A., Hattori T., Kosugi G., Kashikawa N., Inoue K. T., Chiba M., 2007, ApJ, 660, 1016
Treu T., 2010, ARA&A, 48, 87
Tuan-Anh P., Hoai D. T., Nhung P. T., Diep P. N., Phuong N. T., Thao N. T., Darriulat P., 2017, MNRAS, 467, 3513
Vegetti S., Koopmans L. V., 2009, MNRAS, 392, 945
Vegetti S., Czoske O., Koopmans L. V., 2010a, MNRAS, 407, 225
Vegetti S., Koopmans L. V., Bolton A., Treu T., Gavazzi R., 2010b, MNRAS, 408, 1969
Venturini S., Solomon P. M., 2003, ApJ, 590, 740
Vuissoz C. et al., 2007, A&A, 464, 845
Vuissoz C. et al., 2008, A&A, 488, 481
Wambsganss J., 2001, PASA, 18, 207
Warren S. J., Dye S., 2003, ApJ, 590, 673
White S. V., Jarvis M. J., Kalfountzou E., Hardcastle M. J., Verma A., Cao Orjales J. M., Stevens J., 2017, MNRAS, 468, 217
Witt H., Mao S., Schechter P., 1995, ApJ, 443, 18
Wucknitz O., Volino F., 2008, The gravitational lens J1131-1231 — How to miss an opportunity and how to avoid it, Proc. Sci. (IX EVN Symposium), SISSA, Trieste, p. 102
Xu D. D., Mao S., Cooper A. P., Gao L., Frenk C. S., Angulo R. E., Helly J., 2012, MNRAS, 421, 2553
Xu D., Sluse D., Gao L., Wang J., Frenk C., Mao S., Schneider P., Springel V., 2015, MNRAS, 447, 3189
Yang C. et al., 2017, A&A, 608, A144
Yuan T. T., Kewley L. J., Swinbank A. M., Richard J., 2012, ApJ, 759, 66
Zakamska N. L. et al., 2016, MNRAS, 455, 4191
Zheng W. et al., 2012, Nature, 489, 406

This paper has been typeset from a TEX/LATEX file prepared by the author.